Hindawi
International Journal of Intelligent Systems
Volume 2024, Article ID 4108121, 17 pages
https://doi.org/10.1155/2024/4108121

Research Article

Kriging and Radial Basis Function Models for Optimized Design of UAV Wing Fences to Reduce Rolling Moment

Mohammad Hossein Moghimi Esfand-Abadi, Mohammad Hassan Djavareshkian, and Afshin Madani

Department of Mechanical and Aerospace Engineering, Ferdowsi University of Mashhad, Mashhad 9177948974, Iran

Correspondence should be addressed to Mohammad Hassan Djavareshkian; javareshkian@um.ac.ir

Received 18 May 2023; Revised 13 February 2024; Accepted 16 February 2024; Published 27 February 2024

Academic Editor: Vasudevan Rajamohan

In the present study, the effects of the wing fence on the wing tip vortices and control surfaces located at the tip of the wing in a flying wing aircraft have been investigated using a numerical method. For the size of the fences, the average dimensions extracted from the wing tip vortices at different angles of attack are used. The basic determining parameter is the rolling torque coefficient, which is tried to be shown by employing a parametric study of the flow behavior in different situations of fence placement. These effects on the rolling torque of the aircraft are measured due to the presence of the split drag rudder control system. In this study, the fences were installed at three different heights and three different positions along the length of the wing, which were investigated at angles of attack of 7 to 16 degrees. The next stage of the research is to design the dimensions of the fence using the single-objective optimization method (a method to find the best solution for a problem with a specific goal). The designing of the fences at three points based on the dimensions of the wing tip vortex is carried out with the computational fluid dynamics (CFD) method (CFD is a computational method that uses physical laws to predict the behavior of fluids.). The aim of this research is to achieve the best design that converges to an optimal solution with minimum time and cost (CFD solution is long). However, CFD analysis requires a lot of computational time. To address this challenge, we employed a hybrid learning model comprising the radial basis function (RBF), a type of artificial neural network, and Kriging, a Gaussian process-based interpolation technique. The dataset for training the hybrid model was obtained from numerical solutions of CFD simulations involving a fence placed at various locations on the wing. Additionally, a genetic algorithm was employed as the optimization method in all instances where it was required. Using the power of machine learning techniques helped us identify the optimal placement of the fence to prevent it from being engulfed by the vortex and to optimize the utilization of the split drag system, yielding significant improvements.

1. Introduction

Today, with the optimization and advancement of UAV technology, a noticeable reduction in human casualties and environmental issues has been achieved. In addition to military purposes, these types of birds have appeared to be very capable and practical in missions such as delivering messages to hard-to-reach areas, urban operations, and investigating and controlling fires. [1]. Due to the increasing use of lambda-shaped wing configurations compared to delta-shaped wings, it is important to investigate the difference in flow behavior in this type of wing. The lambda-shaped wing is a type of delta-shaped wing with a break in the trailing edge, which gives many advantages over the delta-shaped wing. In lambda-shaped wings, the presence of a break in the trailing edge increases the aspect ratio of this type of wing compared to delta-shaped wings. Increasing the aspect ratio will increase the aerodynamic efficiency [2]. Due to the integrity of the geometric structure in the mentioned configuration, the entire body of the aircraft will contribute to the production of drag force. This issue will increase the aerodynamic efficiency [3]. Apart from the aerodynamic advantages, combining an aircraft's wing and body provides various benefits to its structural design. By integrating the

wing and body, thicker beams can be used in the wing during the design process. As a result, there is less need for extra fortifications elsewhere in the aircraft's structure. This leads to lesser weight for the overall aircraft, thus making it more fuel-efficient and less expensive to run. Also, merging the wing and body enhances the stiffness and strength of the aircraft's structure. Thus, it offers better resistance against turbulence and other environmental conditions that could impact its performance. To sum up, integrating the wing and body is a crucial consideration in modern aircraft design. It offers both aerodynamic and structural benefits that can enhance aircraft performance and safety [4]. Predicting and thoroughly verifying the aerodynamic features of an aircraft is crucial during the initial design phase. Furthermore, it is equally important to define the existing aircraft's aerodynamic characteristics. In both scenarios, obtaining the aerodynamic coefficients such as lift, drag, and moment curves plays a vital role in determining the aircraft's stability and performance. Therefore, determining these coefficients is necessary for the proper evaluation of the aircraft's capabilities and limitations regarding speed, manoeuvrability, and fuel efficiency [5]. Several prior studies (references 1–5) have utilized lambda-shaped wings and UAV, providing a foundation for the present investigation.

With the ever-increasing progress of the science of aerodynamics, it uses different ways to increase the control performance of airplanes. In the early 1990s, the United States launched the Innovative Effector Control Program, which aimed to develop and test control systems for drones. This program was divided into two phases. In this research, an analytical and conceptual study was conducted on control effectors, among which common effectors such as flap, elven, and attack edge flap and some other effectors such as split drag radar and all moving wing tips were investigated [6]. A split drag system has been used for side control in some flying airplanes such as the B-2 bomber. This system, which is installed on the trailing edge of the wing located at the tip of both wings, consists of two plates on top of each other, which are deflected upwards and downwards in opposite directions to create drag in one wing, and by creating pressure drag in one wing, the torque produces a circulation [7]. Rajput et al. used the spilled drag system that they created at the tip of the wing of an example of an unmanned aircraft; they tested it using the CFD numerical method, and their results showed a positive effect on the efficiency and linearization of the rotation moment [8]. The authors of (6–8) are relevant to this work because they also look at control surfaces on airplane wings.

Flying-wing airplanes generally have good aerodynamic behavior at low angles of attack (less than 8 degrees), but, at angles of attack greater than 8 degrees, due to the creation of wingtip vortices, the efficiency of control surfaces decreases [9]. There are several methods to solve the problems caused by flow separation and vortices on control surfaces. In general, the aerodynamic equipment for changing the vortices of the wing includes a sinus attack edge wing, winglet, dog tooth, vortex generator, and fence [10]. Barrett and Farrokhi studied the application of the vortex generator on the Naka 4415 air foil and found that, by using the vortex generator design, they can increase the lag angle and drag coefficient. Vortex generators are small blades that are installed on the wing or body of the plane, which is usually designed in the shape of an airfoil or a rectangle. The vortex-generating tool prevents the airflow from separating and being in an aerodynamic stall. In addition to the above, this tool plays a role in improving the performance of the wing and controls surfaces and changes in the wing tip vortices [11]. A practical and more effective way to deal with vortices is wing fences, which have been seen in nature and some birds [12]. Wing fences were invented by Wolfgang Liebe in 1938 to delay the excessive movement of the eddy current along the wing and its rapid increase [13]. The fences can be defined as a plate that is placed on top of the wing surface and in front of the airflow, and depending on its design, it extends to the end edge of the wing [14]. Papadopoulos et al. investigated a prototype of an integrated wing-body UAV with fences on the wings. According to their results, the lift and drag coefficient did not change much up to the angle of attack, of 8 degrees. However, from 8 degrees and above, the coefficient has shown better performance [15]. The fences direct the vortices formed on the wing to the rear and towards the trailing edge and cause the outer parts of the wing not to have problems in producing drag [16]. The studies presented in (9–16) align with the present investigation in their exploration of vortex phenomena on aircraft wings and the potential for vortex control devices.

Decision-making in every engineering project should be accompanied by logical and scientific reasoning and analysis; therefore, optimization methods can be used to ensure the decisions made or to improve them. Over the past forty years, countless algorithms have been developed to find solutions to various optimization problems; these algorithms are mainly based on linear and nonlinear programming methods.

Esfahanian et al. proposed an alternative deep-learning model to optimize the design of a two-stage axial turbine with 112 geometric parameters. They concluded that this method significantly reduces the computational cost, making it 100,000 times faster, while achieving high accuracy [17]. In 2024, Li et al. introduced IR-SAEA, a new surrogate-assisted evolutionary algorithm designed to handle high-dimensional and computationally expensive multiobjective optimization problems. This algorithm uses a hybrid model of radial basis function (RBF) and inverse distance weighted (IDW) models to effectively approximate the true objective functions. The authors concluded that the model produced not only predicted target values but also valuable uncertainty information. This additional information facilitates a more informed exploration-exploitation balance by employing a lower confidence constraint filling criterion in the algorithm [18]. The genetic algorithm was developed by John Holland in 1960 and was developed for the first time in 1975 when many improvements were made by Pazooki et al. [19]. The genetic algorithm starts with a random generation or initial population, and then, it is repeated with selection, reproduction, and mutation processes and evaluation of the objective function or the cost function until the final generation is reached. However, optimization using the mentioned methods is difficult in many industrial applications. Almost everything that engineers design involves

multiple objectives, where two or more conflicting objectives may be interrelated to reach optimal decisions [19]. In the field of aerodynamic and structural analysis using the multiobjective optimization method, we can refer to the actions of Perez et al. and his colleagues in 2008 [20]. In 2005, Ghorbani and Malaek designed and optimized a short landing and takeoff aircraft using a genetic algorithm [21]. In 2010, Yoon et al. and his colleagues implemented a multiobjective design optimization method for a general aviation aircraft by modeling issues such as aerodynamics, propulsion, mission, weight, stability, control, and performance [22]. Aerodynamic modeling methods can be challenging to meet design requirements. However, using the Kriging algorithm for creating an aerodynamic model is a highly targeted approach that addresses specific aerodynamic characteristics. In general, the Kriging model is more precise and easier for nonlinear approximation, making it a useful tool for accurately predicting aerodynamic performance. By implementing the Kriging algorithm, engineers can improve the accuracy of their aerodynamic models and optimize the aircraft's design parameters accordingly. This results in improved aircraft performance, fuel efficiency, and safety during flight. Therefore, the use of the Kriging algorithm is an effective solution for designing and evaluating aircraft with complex aerodynamic characteristics [23]. Kriging usually performs better than other interpolation methods because it takes into account the way a feature varies in space through the semivariogram. A semivariogram is a representation of the spatial correlation between data points, illustrating how closely they tend to resemble each other as their distance from each other increases [24]. Stochastic models and Kriging were developed by Georges Matron at his research center in 1968 [25].

Petcharat et al. proposed a multiobjective optimization method, combining the nondominated sorting genetic algorithm II (NSGA-II) with the Kriging model, to determine the 3D printing parameters for onyx/carbon fiber composites that achieve the desired mechanical properties. This approach significantly reduces the need for physical testing, as demonstrated by the successful achievement of good and favorable results with minimal experimentation [26].

Zhao et al. optimized the circulation and rotation and rolling coefficients of combining existing control surfaces on the leading edge using the Kriging method [27]. Namura et al. used the Kriging method to optimize the vortex generators on the wing of the aircraft to maximize the Bera coefficient [10]. Building upon the optimization methods presented in (17–29) and prior works, this article proposes a novel approach to address the aforementioned issue.

The existence of a split drag rudder control system is to create Yawing torque for the plane. To purify the Yawing torque, we neutralize the rolling torque. In normal airplanes, the Yawing torque we have also has a disturbing rolling torque. The most disturbing parameter that affects the Yawing is the rolling torque, which we tried to neutralize. This research aims to design the dimensions of the fence to reduce the rolling moment to achieve the best design that converges to an optimal solution with minimum time and cost. The design of the fences in three points is carried out based on the dimensions of the wingtip vortex with the CFD method. However, CFD analysis requires a large amount of computational time. To solve this problem by using two types of Kriging model and RBF and eventually genetic algorithm, through placing the initial conditions of the problem and the results of a numerical solution when there are fences, the rolling moment coefficient is minimized by specifying the most suitable location of the fence on the wing.

2. Main Method

This research utilizes the Kriging method and genetic algorithm for optimization. The first step in optimization involves identifying objective functions, optimization variables, and calculating the values of objective functions based on design variables. In this case, the rolling torque is the objective function, and length variables, width, height, and distance from the center of the fence to the nose of the plane are the optimization variables. As there is no specific relationship defined among these variables, the Kriging method is used to establish the necessary relationships. Fences installed on the UAV's wing serve to reduce the rolling moment. The objective function is evaluated using Kriging-based alternative models that estimate function values and approximate errors to locate further sample points and improve accuracy. The genetic algorithm, then, examines optimal solutions using the estimated function values and approximation errors for each objective function. The research starts with simulating the UAV in various angles of attack, determining vortex passage location and dimensions, and defining initial fence placement coordinates based on the wing's vortex length and diameter using geometry production software. In the second step of the simulation of the UAV with the fences on the wing, the CFD method is used to obtain the rolling torque. The first step involves establishing a relationship between input parameters and the objective function. The second step consists of using the genetic algorithm to optimize the objective function and select additional sample points from the resulting optimal solutions. In the third step, these newly chosen sample points are used to update the Kriging model. The genetic algorithm then reexamines the updated model's optimal solutions. This iterative process continues (as illustrated in Figure 1) until the sample points appropriately match the expected problem characteristics.

2.1. Learning Section

2.1.1. General, Comprehensive, and Simple Explanation of Three Kriging, RBF, and Genetic Algorithm Models

(1) Genetic Algorithm

(1) Start with a population of creatures with random genes
(2) Evaluate their performance using a fitness function
(3) Select the fittest creatures as parents for the next generation
(4) Create new offspring by combining the genes of the selected parents (crossover)

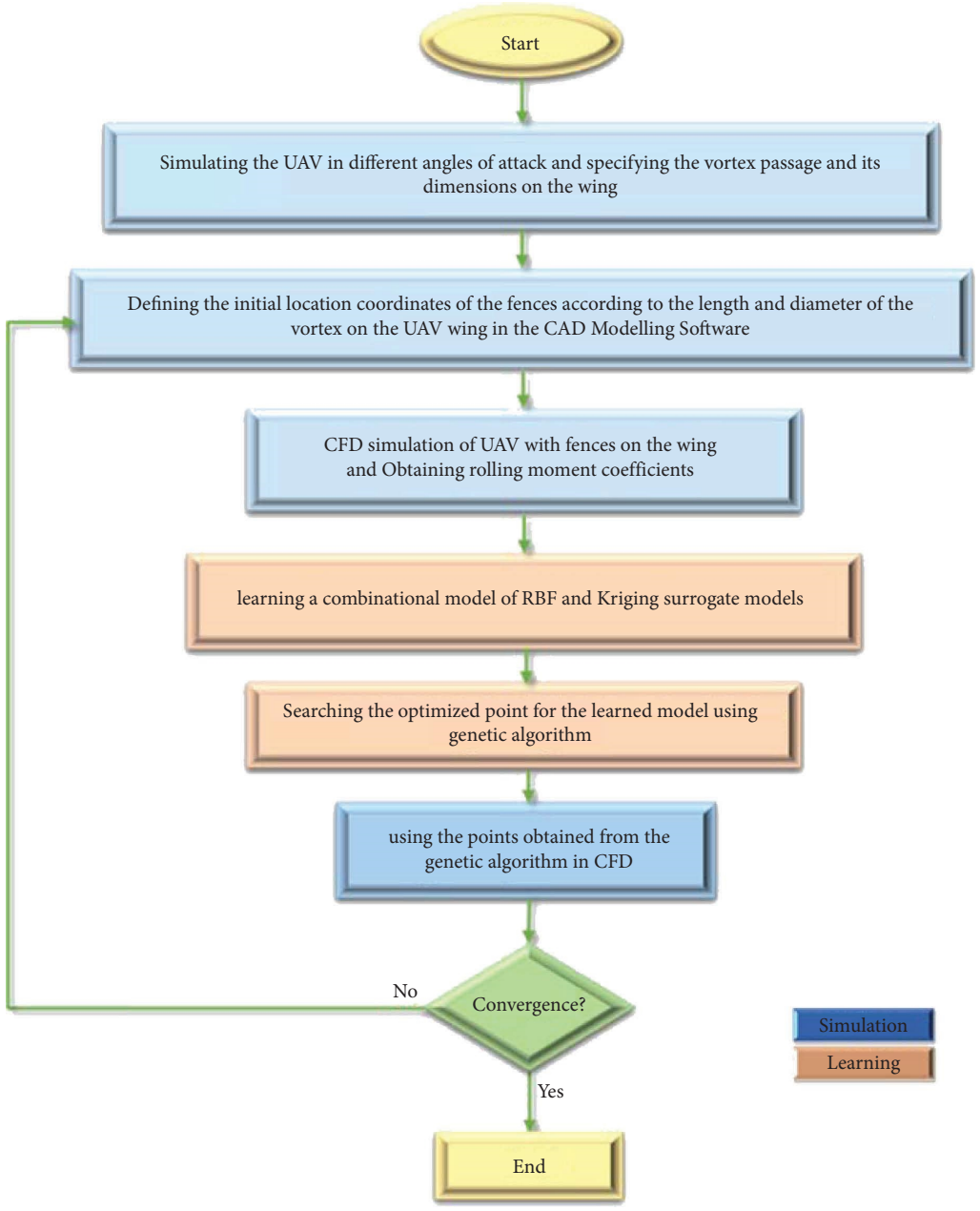

Figure 1: Flowchart of optimization and solution process.

(5) Occasionally introduce small random changes in the genes (mutation)

(6) Repeat steps 2 to 5 for multiple generations

(7) Over time, the population evolves and becomes better adapted to solve the problem

By iterating this process, the genetic algorithm helps us find better and better solutions over time, as the fittest creatures reproduce and pass down their advantageous genes to future generations.

(2) Kriging. The Kriging model is a statistical technique that helps us make predictions or estimates of unknown functions based on observed data points. It is often used when we have limited data and want to understand the behavior of a function at unobserved locations. Imagine you have a bunch of points on a graph, where each point represents an input location (x) and has a corresponding output value (y). The goal is to estimate what the function looks like and predict the output values at new locations on the graph.

The Kriging model uses two important concepts:

(1) Trend:

The model assumes that the unknown function has a trend or a general pattern across the input space. This trend can be a straight line, a curved shape, or

even more complex. The trend captures the average behavior of the function.

(2) Variability:

The model recognizes that the function's values might vary around this trend. In other words, there could be fluctuations or differences between the observed output values at different locations. These variations are measured through a concept called covariance.

The Kriging model combines the trend and the variability to make predictions and estimate uncertainty. It does this by capturing the relationships among different data points based on their locations and output values. Essentially, the Kriging model creates a statistical model that represents the unknown function based on the observed data. This model takes into account the observed values, the trend, and the relationships among data points to make predictions at new locations. Overall, the Kriging model helps us approximate and understands unknown functions using a combination of trends, variability, and statistical relationships among observed data points.

The Kriging model represents the unknown function $y\,(x)$ as follows:

$$y(\mathbf{x}) = \mu(\mathbf{x}) + \varepsilon(\mathbf{x}). \tag{1}$$

The variable x represents a vector with n dimensions, where each dimension corresponds to a specific design variable. These variables may include length, width, height, and the distance between the center of the fence and the nose of the plane. $y\ (\mathbf{x})$ is the unknown function being represented, and the function $\mu\ (\mathbf{x})$ represents a general model, while the function $\varepsilon\ (\mathbf{x})$ indicates the local deviation from this model. In the local deviation model, the value of an unknown point $\mathbf{x}$ is described using a stochastic process. Gaussian random functions are used as correlation functions to interpolate sample points and estimate trends in random processes. This statement explains that the correlation between $\varepsilon(\mathbf{x}^i)$ and $\varepsilon(\mathbf{x}^j)$ is strongly influenced by the distance between the corresponding points $\mathbf{x}^i$ and $\mathbf{x}^j$. In a Kriging model, a weighted interval is used instead of the Euclidean interval to calculate distance because the weighted interval treats all design variables equally. The function of the distance between points $\mathbf{x}^i$ and $\mathbf{x}^j$ is expressed as equation (2), the correlation between points $\mathbf{x}^i$ and $\mathbf{x}^j$ is expressed as equation (3), and the predicted value by the Kriging model is expressed as equation (4).

$$\mathrm{dis}\left(\mathbf{x}^i, \mathbf{x}^j\right) = \sum_{k=1}^{m} \theta_k \left| x_k^i - x_k^j \right|^2, \tag{2}$$

$$\mathrm{Corr}\left[\varepsilon\left(\mathbf{x}^i\right), \varepsilon\left(\mathbf{x}^j\right)\right] = \exp\left[-\mathrm{dis}\left(\mathbf{x}^i, \mathbf{x}^j\right)\right], \tag{3}$$

$$\widehat{y}(x) = \widehat{\mu}(x) + r^T R^{-1}(y - \widehat{\mu}). \tag{4}$$

To derive the final equation of (4), we can start using the best linear forecast problem. The measurements vector $y = \left(y(\mathbf{x}_1) \ \cdots \ y(\mathbf{x}_n)\right)^T$ and a CFD output calculation at the locations $\left[\mathbf{x}_1 \ \cdots \ \mathbf{x}_n\right]$ are considered realizations of real-valued random variables $\left[Y(\mathbf{x}_1) \ \cdots \ Y(\mathbf{x}_n)\right]$.

Kriging answers the task, a predictive value $\widehat{y}(\mathbf{x})$ in an unobserved place x based on observed measured values $\left[y(\mathbf{x}_1) \ \cdots \ y(\mathbf{x}_n)\right]$ at the places $\left[(\mathbf{x}_1) \ \cdots \ (\mathbf{x}_n)\right]$ to specify.

In the best linear forecast problem, the predictive value $\widehat{y}(x)$ at a new place x has a linear formation like equation (5) with the weights of $[a_0, a_1, \ldots a_n]$.

$$\widehat{Y}(x) = a_0 + \sum_{i=0}^{n} a_i Y(x_i). \tag{5}$$

To obtain the optimal weights, we employ the mean square forecast error (MSE), as shown in equation (6), which represents the expected value of the $(\widehat{\mathrm{Y}}(\mathbf{x}) - \mathrm{Y}(\mathbf{x}))^2$ random variable.

$$\mathbb{E}\left[(\widehat{Y}(\mathbf{x}) - Y(\mathbf{x}))^2\right]. \tag{6}$$

Indeed, the best weights can be calculated using the optimization of equation (7).

$$(a_0^*, a_1^*, \ldots, a_n^*) = \underset{(a_0, a_1, \ldots, a_n)}{\mathrm{argmin}} \ \mathbb{E}\left[\left(a_0 + \sum_{i=1}^{n} a_i Y(\mathbf{x}_i) - Y(\mathbf{x})\right)^2\right]. \tag{7}$$

The answer to equation (7) optimization for the vector of $A = (a_1^*, \ldots, a_n^*)^T$ is as follows:

$$A^T = r^T R^{-1}. \tag{8}$$

Also, the answer for a_0^* is as follows:

$$a_0^* = \mu_0 - A^T \widehat{\mu}. \tag{9}$$

That μ_0 is the expected value of the random variable of $Y(\mathbf{x})$. Also, $\widehat{\mu} = (\mu_1, \ldots, \mu_n)^T$ is a $(n \times 1)$ vector that each μ_i is the expected value of the random value of $Y(\mathbf{x}_i)$.

By substituting equations (8) and (9) into equation (5), we can obtain the best linear predictive value.

$$\widehat{y}(x) = a_0^* + \sum_{i=0}^{n} a_i^* y(x_i) = \mu_0 - A^T \widehat{\mu} + A^T y = \mu_0 + r^T R^{-1}(\mathrm{y} - \widehat{\mu}). \tag{10}$$

Also, y is the measurements vector that was defined previously.

In equation (10), $\widehat{y}(x)$ represents the predicted value by the Kriging model, $\widehat{\mu}(x)$ is the estimated value of μ (**x**), R represents the $n \times$ n symmetric matrix whose entry (i, j) is Corr [$\varepsilon(\mathbf{x}^i)$, $\varepsilon(\mathbf{x}^j)$], ($r$) is a vector whose i-th element is $r_i(x) = \text{Corr}\ [\varepsilon(\mathbf{x}^i), \varepsilon(\mathbf{x}^j)]$, and $y(x)$ and $\widehat{\mu}(x)$ are expressed as equation (11) for (n) sample points, where (y) is the output variable and $\widehat{\mu}(\mathbf{x})$ is obtained from equation (14). The unknown parameter θ_k for the Kriging model can be estimated by maximizing the exponential function given in equation (12). Maximizing the likelihood function is a nonlinear optimization problem. In this research, a genetic algorithm (GA) is used to solve this problem. For certain (θ), $\widehat{\sigma}^2$ can be defined as equation (13).

$$\begin{aligned} \mathbf{y} &= \left[y\left(\mathbf{x}^1\right) \ \cdots \ y\left(\mathbf{x}^n\right)\right], \\ \hat{\boldsymbol{\mu}} &= \left[\widehat{\mu}\left(\mathbf{x}^1\right) \ \cdots \ \widehat{\mu}\left(\mathbf{x}^n\right)\right], \end{aligned} \tag{11}$$

$$\text{Ln}\left(\widehat{\mu}, \widehat{\sigma}^2, \boldsymbol{\theta}\right) = -\frac{n}{2}\ln\left(\widehat{\sigma}^2\right) - \frac{1}{2}\ln\left(|R|\right), \tag{12}$$

$$\widehat{\sigma}^2 = \frac{(\mathbf{y} - \widehat{\mu})^T \mathbf{R}^{-1} (\mathbf{y} - \widehat{\mu})}{n}. \tag{13}$$

Then, if the normal Kriging model is used, $\widehat{\mu}(\mathbf{x})$ constant value is assumed, which is expressed as equation (14). In addition, since the random variables $[Y(\mathbf{x}_1) \ \cdots \ Y(\mathbf{x}_n)]$ have a covariance matrix, we can employ the generalized least squares (GLS) method to estimate the parameter μ_0. The estimated value will be identical to the value obtained from equation (14).

Conventional Kriging considers the hybrid model that uses the RBF network to approximate the overall model, and $\widehat{\mu}(\mathbf{x})$ is defined as the RBF output. ($\widehat{y}(x)$) is displayed as equation (15). Where w_0 is the average value of the sample points, (w_i) is the weight of the i-th function and hi(x), and the number of basic functions is the same as the number of sample points (n). In equation (16), φ indicates the function used, (c^i) is the center, and (r_i) is the width (the design variables must be normalized). Gaussian function (z) = exp ($-$z^2) is used in this research. The value of (r_i) controls the superposition of functions that should be set. On the other hand, w_i is determined by minimizing the Herring function given in equation (17). λ_i is a tuning parameter for w_i.

$$\widehat{\mu}(\mathbf{x}) = \frac{\mathbf{1}^{\mathrm{T}}\mathbf{R}^{-1}\mathbf{y}}{\mathbf{1}^{\mathrm{T}}\mathbf{R}^{-1}\mathbf{1}}, \tag{14}$$

$$\widehat{y}_{\text{RBF}}(\mathbf{x}) = w_0 + \sum_{i=1}^{n} w_i h_i(\mathbf{x}), \tag{15}$$

$$h_i(\mathbf{x}) = \varphi\left(\frac{\|\mathbf{x} - c_i\|}{r_i}\right). \tag{16}$$

Figure 2 shows a diagram of a radial basis function (RBF) network with one hidden layer. In this network, inputs are fed into the input layer and then processed through connections between neurons in the input layer and the hidden layer. The outputs of the hidden layer are then passed to the output layer. In Figure 2, the input layer has three neurons, and the hidden layer has two neurons. The weights between the neurons are shown by the numbers on the lines. The way this network works is that the inputs are fed into the input layer and then processed through the connections between neurons in the input layer and the hidden layer. This processing involves applying a nonlinear function to the sum of the weighted inputs and the bias of the neuron. The outputs of the hidden layer are then passed to the output layer. In this layer, the outputs of the hidden layer are again processed through a nonlinear function to produce the final output of the network. In this figure, the nonlinear function used in both the input and hidden layers is the radial basis function (RBF). The radial basis function is a nonlinear function that is shaped like a radial function.

$$E = \sum_{i=1}^{n} \left(y\left(\mathbf{x}^i\right) - \widehat{y}_{\text{RBF}}\left(\mathbf{x}^i\right)\right)^2 + \sum_{i=1}^{n} \lambda_i w_i^2. \tag{17}$$

Certainly, in a Kriging model, the accuracy of predictions for function values depends primarily on how far the point was analysed in the sample points. The closer the point (x) is to the available sample points, the more accurate the prediction of $\widehat{y}(x)$ will be. This challenge is expressed mathematically in the following equation:

$$S^2(x) = \widehat{\sigma}^2\left[1 - r^T R^{-1} r + \frac{\left(1 - 1^T R^{-1} r\right)^2}{1^T R^{-1} 1}\right]. \tag{18}$$

This statement explains that s^2 (x) is a measure of the uncertainty of an estimated value at point x, calculated using mean squared error. If the accuracy level provided by a surrogate model is found to be inadequate, it may require building a new model with additional sample points to improve its performance. The ultimate goal is to obtain a surrogate model that provides accurate predictions to inform decision-making.

(3) Flowchart Steps in Figure 3

Data Acquisition:

The process starts with acquiring a dataset of input vectors (denoted by x) and corresponding output values (denoted by y). Each input vector x contains information about relevant design variables, such as distance from the longitudinal axis, fence length, distance between the fence and the UAV nose, and fence height, and output vector y contains the rolling moment coefficient.

Kriging Model Branch:

A Kriging model is constructed using the acquired dataset. A genetic algorithm is employed to minimize the cost function associated with the Kriging model, resulting in estimated (θ) parameters. Reference is made to the Kriging cost function (likelihood).

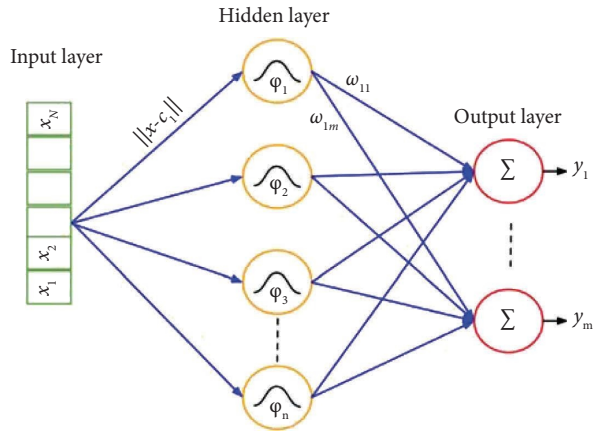

Figure 2: Diagram of a radial basis function (RBF) network with one hidden layer.

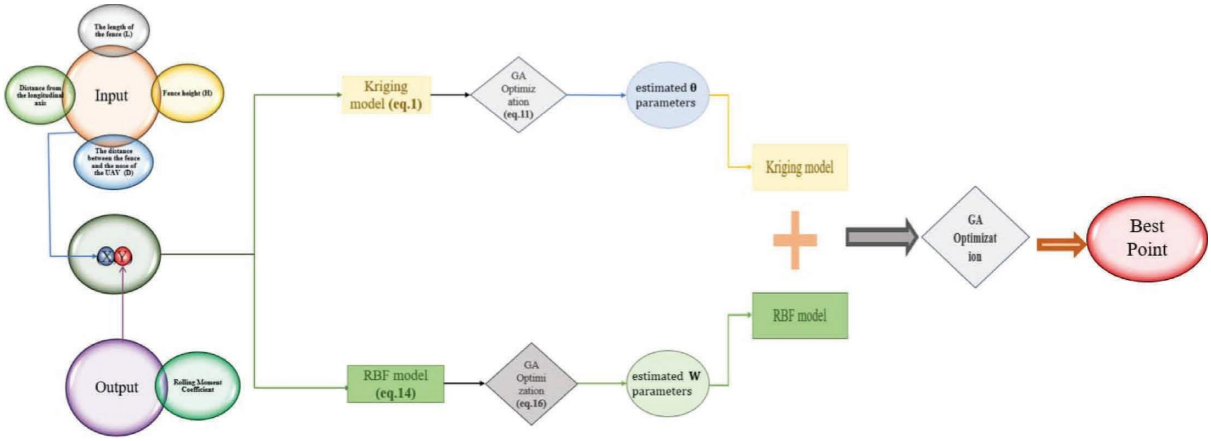

Figure 3: This flowchart depicts an algorithmic framework for estimating optimal design variables within the context of the current problem.

RBF Model Branch:

An RBF neural network model is created using the same dataset. The genetic algorithm is again utilized to optimize the model's parameters, leading to estimated (**w**) parameters. Reference is made to the RBF-related cost function.

Model Combination:

The Kriging and RBF models are combined to form a new, enhanced model by summing their outputs.

Genetic Algorithm for Optimal Point:

The genetic algorithm is applied to the combined model to identify the input vector x that produces the optimal output value.

Output and Potential Applications:

Model Improvement: It can serve as a new data point to further refine and improve the Kriging and RBF models through another iteration of the flowchart.

2.2. CFD Simulation

2.2.1. The Geometry under Consideration. The model used in this test is a swing-shaped lambda flying-wing UAV. This UAV is designed with a wingspan of 1 meter and a 56-degree turning angle. The said UAV has been investigated in limited numerical and experimental tests. The geometry of this UAV is obtained from [28]. In this type of UAV, a break in the trailing edge of the wing is used, which is why this configuration is named lambda shape. The control system created in this UAV to produce rotational torque is the split drag system. This system is made up of two plates on top of each other, and with the deviation of both plates, pressure drag is created in one of the wings and creates a rotational torque. The dimensions of this system along with the overall dimensions of the UAV are shown in Figure 4. Also, in this image, the location of the fence is specified. In the entire test process, to reduce the number of calculations, the maximum opening angle of the split drag has been used. Therefore, the opening angle of the split drag system has been fixed and symmetrical to 30 degrees up and 30 degrees down. In the numerical calculations, first, the location of the fence and the height of the fence, each in three different sizes and three different positions, were drawn and created, and, finally, these designs were numerically tested separately.

2.2.2. Fence Design. In airplanes with a high backward angle, a vortex called the wing tip vortex is formed, which extends in a conical form from the wing root area at the leading edge

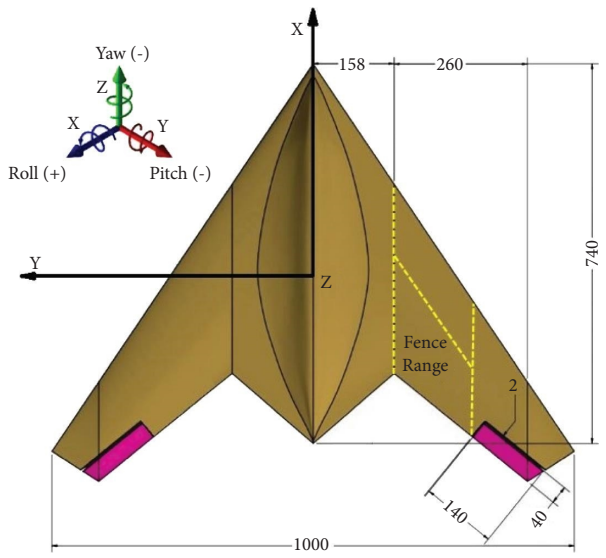

Figure 4: The view from the top of the swing UAV along with the dimensions of different parts.

to the wing tips. This vortex will be examined further. The location and height of the fences were designed based on the average dimensions of the length of the cross section and the height of the wingtip vortex at angles of attack s of 10, 13, and 16 degrees. The length of the cross section of the vortex is measured in three parts: the beginning, the middle, and the end of the vortex, and the length of the fences will be considered equal to the length of these sections in each part. The height of the fences is also considered as a percentage of the height of the vortex in the mentioned sections. This percentage of the height and length of the fences is given in Table 1.

In Figure 5, a view of the fences created on the wing of this UAV can be seen in three positions A, B, and C at a height of 70%.

3. Solution Method and Domain

The created mesh is the unstructured type and was carried out by Ansys Meshing 2015 software. The mesh is finer as it gets closer to the surface of the UAV, and it is also finer with a coefficient of fineness in the corners. Also, to increase the accuracy of the solution, the mesh in an elliptical volume around the model has been made smaller and its number has been increased. According to the speed of the flow and the diameter of the boundary layer, the boundary layer mesh has been created on the entire surface of the UAV. The boundary layer mesh is made of 10 layers with the height of the first cell being 0.00034 meters, which is equivalent to the dimensionless number Y^+ 22. Regarding the selection of the k–ω–SST turbulence model, the selection of this value for the (Y^+) number of Mehrezak has been accepted according to the authors of [29]. In Figure 6, a comprehensive visual presentation of multiple perspectives and intricate details regarding the solution method (meshing) employed in addressing the given problem is meticulously depicted.

Due to the open drag split in the left wing, and the asymmetry between the sides of the UAV, the entire UAV is modelled. The boundary conditions defined on the surfaces of the solution domain are as follows: the inlet velocity at the front and bottom boundary of the domain is equal to 30 m/s, the outlet pressure boundary at the top and back of the domain is equal to the static pressure, and the boundary condition is symmetrical on both sides of the solution domain. In Figure 7, the dimensions and form of the solution domain can be seen.

To determine whether the results are dependent on the number of cells in the mesh, the drag coefficient is compared for different numbers of mesh. In Figure 8, from point named 4 onwards, the changes in the drag coefficient become very small. Therefore, grid 5 with the amount of 5850000 cells will be suitable for this research in terms of volume and accuracy.

4. Validation

For validation purposes, the numerical lift and drag coefficients have been compared with the experimental results obtained from the reference wind tunnel [29] at a speed of 30 m/s in different angles of attack s (Figure 9). This comparison shows that the results are obtained with little difference compared to the experimental results. The highest percentage of difference is 4.9 percent in the forward coefficient and 4.6 percent in the backward coefficient.

5. Results and Discussion

After obtaining the dimensions of the wing tip vortex and the design of the fences, the UAV will be tested in the condition where the left drag split is opened at an angle of 30 degrees. Furthermore, the produced fences will be placed on the model in the announced positions from Table 1, and the simulation will be executed. The purpose of creating fences on the wing is to reduce the effect of the wingtip vortex on the split drag rudder system at high angles of attack s (due to the increase in the diameter of the vortex). The upper surface of the split drag system has lost its efficiency due to being inside the swirling vortex flow of the wing tip and has failed to produce negative lift force in order to neutralize the force generated from the lower plane. The presence of the fence on the wing leads the vortices to go down, reduces the effect of the vortex on the upper surface of the drag split, and compensates for a part of the negative drag force lost on the upper surface.

Figure 10 shows the roll torque coefficient according to the angle of attack for different heights of fence C.

The presence of the fence on the wing has been able to reduce the amount of roll torque. With the increase in the height of the fence, a more suitable performance of the split drag system has been observed in reducing the rolling torque. With the increase of the angle of attack by 16 degrees due to the larger size of the vortex, the 30% and 50% fences have not been able to eliminate the effect of this vortex on the split drag, and, for this purpose, the high fence has performed 70% better. For this purpose, in positions A and B,

Table 1: The dimensions of the fence extracted from the dimensions of the wingtip vortex in millimetres.

The height of the fence (H)			The length of the fence (L)	The name of the location of the fence relative to the longitudinal axis of the UAV (distance value)
70%	50%	30%		
7	5	3	49	A (158)
14	10	6	144	B (234)
22.4	16	9.6	172	C (310)

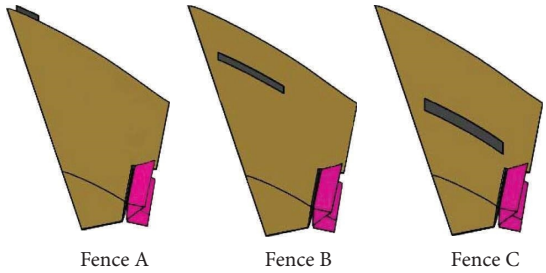

Figure 5: The left wing of the UAV shows the location of the fences at a height of 70% to prevent vortices.

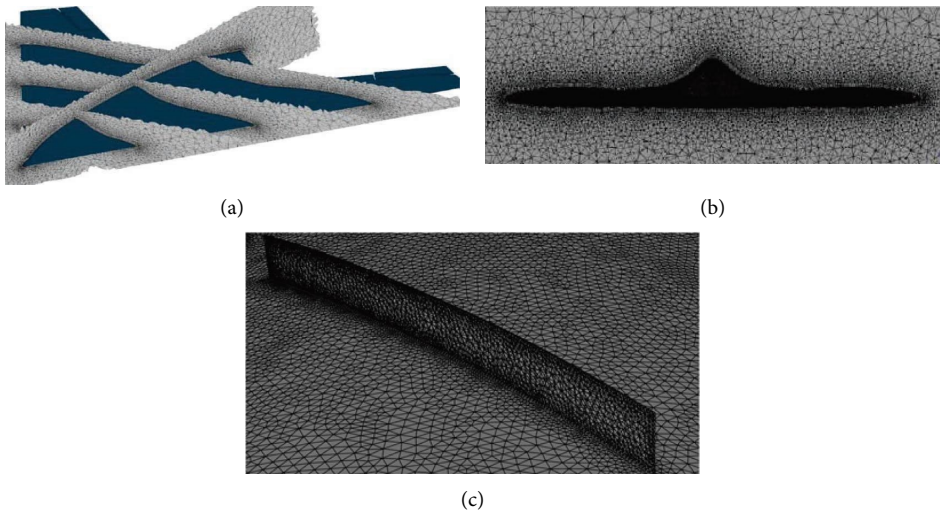

Figure 6: Views of the solution created in this research: (a) cut view of the mesh around the model, (b) cut section of the view facing the model, and (c) mesh around the fence and on the wing UAV.

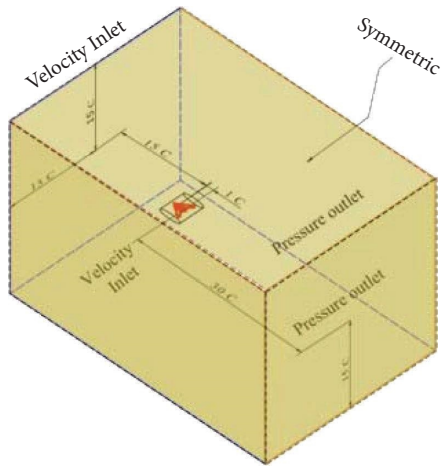

Figure 7: Resolution domain and its dimensions relative to the average chord length of the wing.

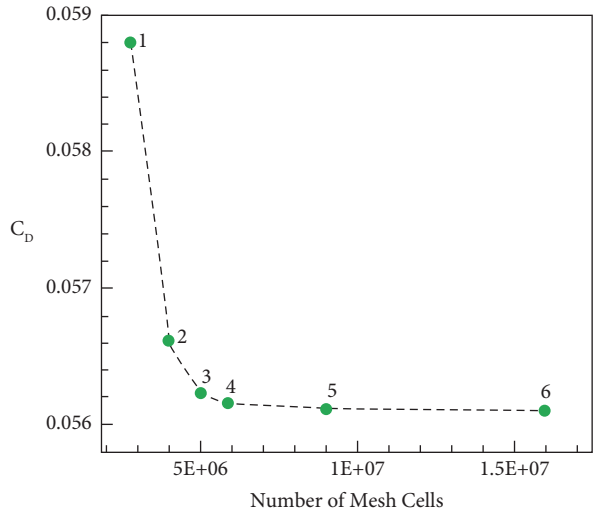

Figure 8: Mesh independence diagram.

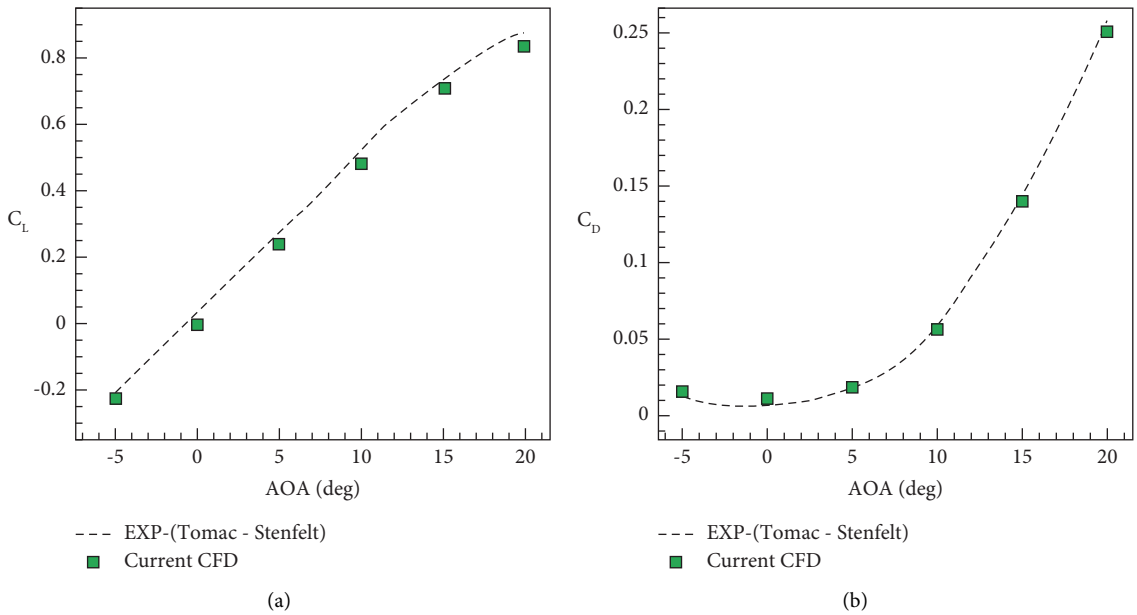

Figure 9: Comparison of the present numerical results with experimental data [29]: (a) lift coefficient and (b) drag coefficient.

changes in the height of the fence had a smaller effect on the roll torque coefficient, which is shown in Figures 11 and 12.

In the algorithm explained in part (2), we optimize the fences on the wing of the airplane. At the angle of attack between 7 and 13, because the vortices at the tip of the wing are not very large, it is clear according to the design of the fences and the shape of Figure 13 that the closer the fence is to the split drag, the lower the rolling coefficient.

Figure 14, a rectangle in shape, depicts the relationship between the UAV design and the rolling moment coefficient using a parallel coordinate diagram. It illustrates the interplay between the input parameters (distance from the longitudinal axis, fence length (L), the distance between fence and nose (D), and fence height (H)) and the output parameter the rolling moment coefficient. Notably, fences A, B, and C are positioned at a 16-degree angle of attack (AOA). This specific angle is presented because the optimization process solely focused on this condition.

We optimized the fences of 30%, 50%, and 70% of the vortex diameter at the angle of attack of 16 degrees, because, at a lower angle of attack, the closer we get to the split drag, the better the result. At the angle of attack of 16 degrees, due to the large vortex, the results fluctuated, so we optimized the fence for better performance. Optimization has been carried out on 30, 50, and 70% (**P**), but, due to similarity and better understanding, the 30% optimization chart has been displayed in full.

Figure 15 represents equation (14) after applying the learning algorithm showing a local deviation model. Figure 15(a) corresponds to C_l according to distance from the

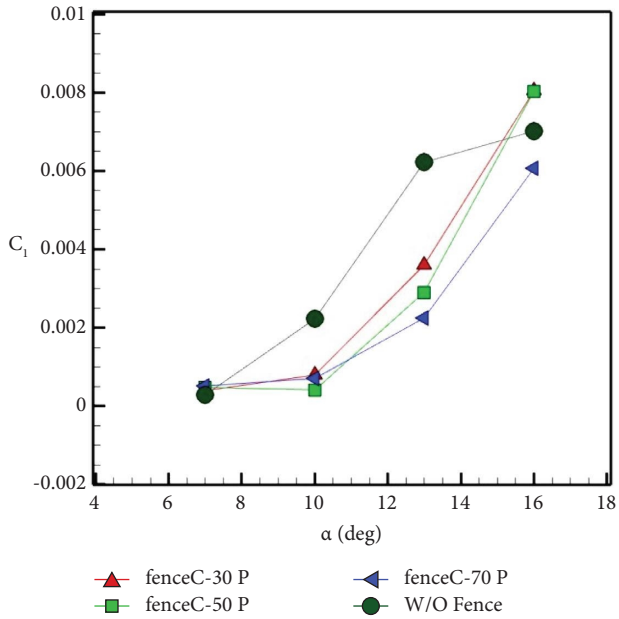

Figure 10: The moment coefficient of roll fence C with different heights.

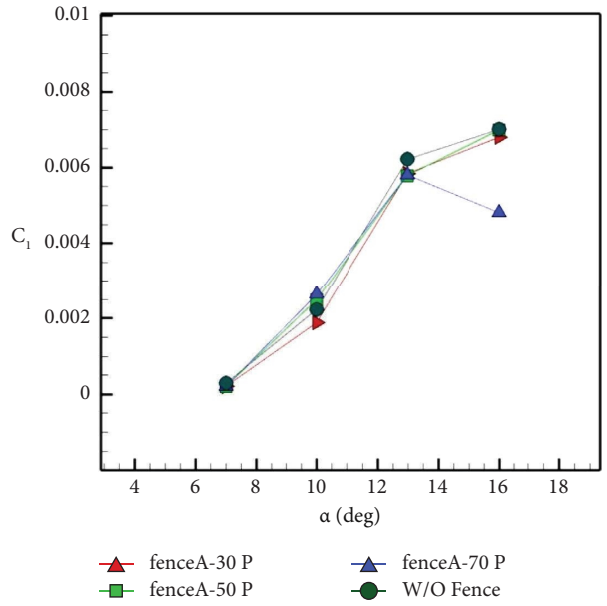

Figure 11: The moment coefficient of roll fence A with different heights.

longitudinal axis and H. Figure 15(b) corresponds to C_l according to D and L. Figure 15(c) corresponds to C_l according to L and distance from the longitudinal axis.

In Figure 16, equation (15) is observed after applying the learning algorithm, which shows the global model. Figure 16(a) corresponds to C_l according to distance from the longitudinal axis and H. Figure 16(b) corresponds to C_l according to D and L. Figure 16(c) corresponds to C_l according to L and distance from the longitudinal axis.

In Figure 17, Figure 17(a) corresponds to C_l according to distance from the longitudinal axis and H. Figure 17(b) corresponds to C_l according to D and L. Figure 17(c) corresponds to C_l according to L and distance from the longitudinal axis. As per step 5 of the flowchart, after applying the genetic algorithm to the functions learned in the previous step (as shown in diagrams in Figure 17), the minimum value of the roll coefficient is obtained. After determining the optimal roll coefficient, this new point is set for simulation according to step 6 of the flowchart. It is used in CFD simulations. Table 2 shows the exact dimensions of the fences created on the UAV wing at three different heights and the optimized point (O).

Table 2 shows the characteristics of the placement of the fence on the wing in positions A, B, C, and O (optimized point 30% P, 50% P, and 70% P), and Figure 18, for example, shows the location of the fences (30% P) on the wing in positions A, B, C, and O.

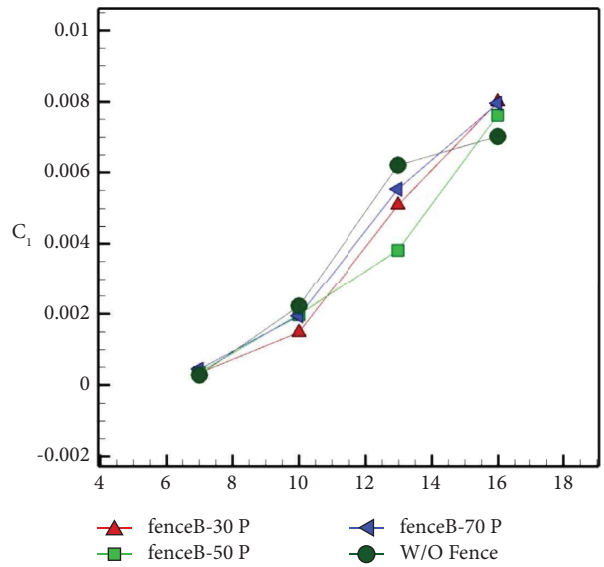

Figure 12: The moment coefficient of roll fence B with different heights.

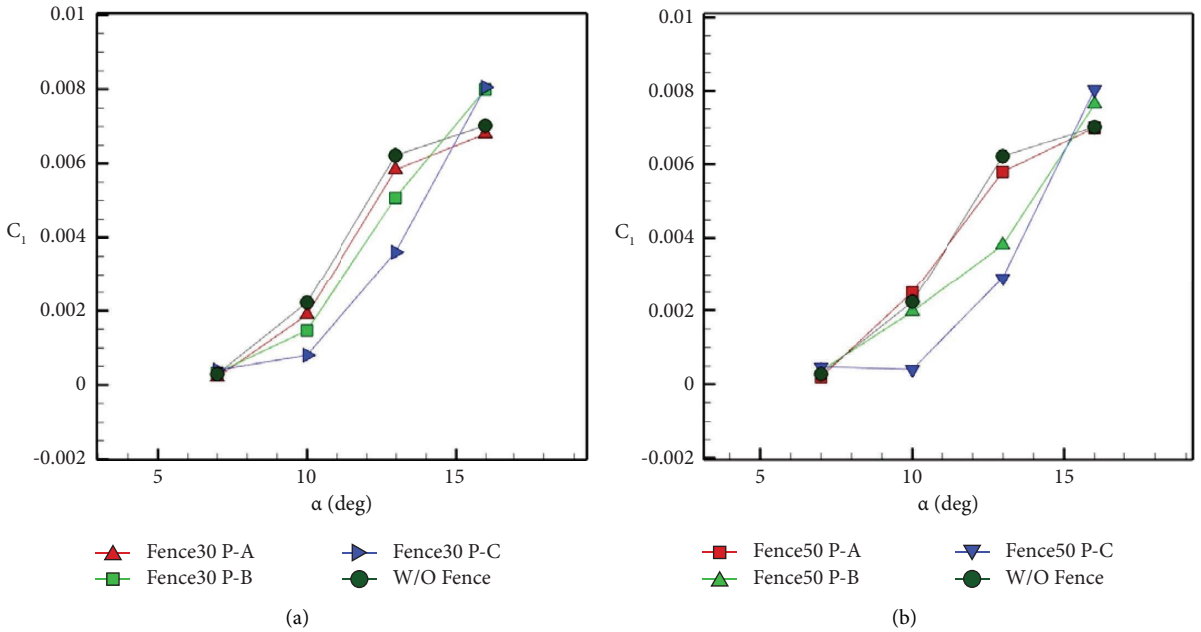

Figure 13: Continued.

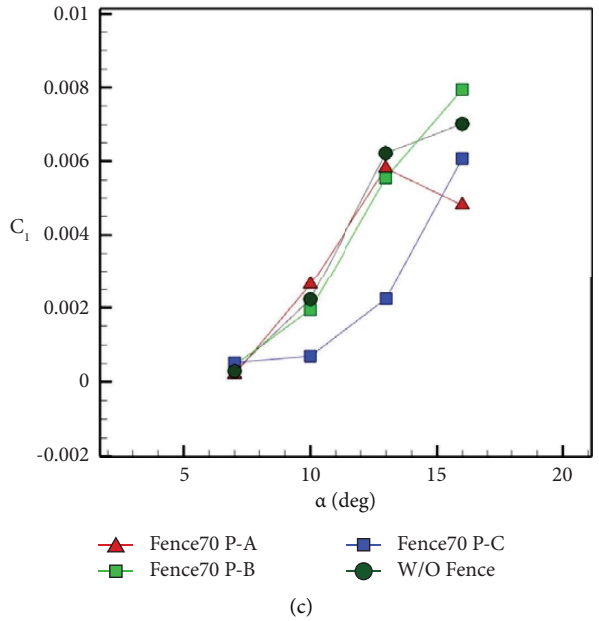

(c)

Figure 13: Diagram showing different angles of attack *s* in different fence positions: (a) 30% of the vortex diameter, (b) 50% of the vortex diameter, and (c) 70% of the vortex diameter.

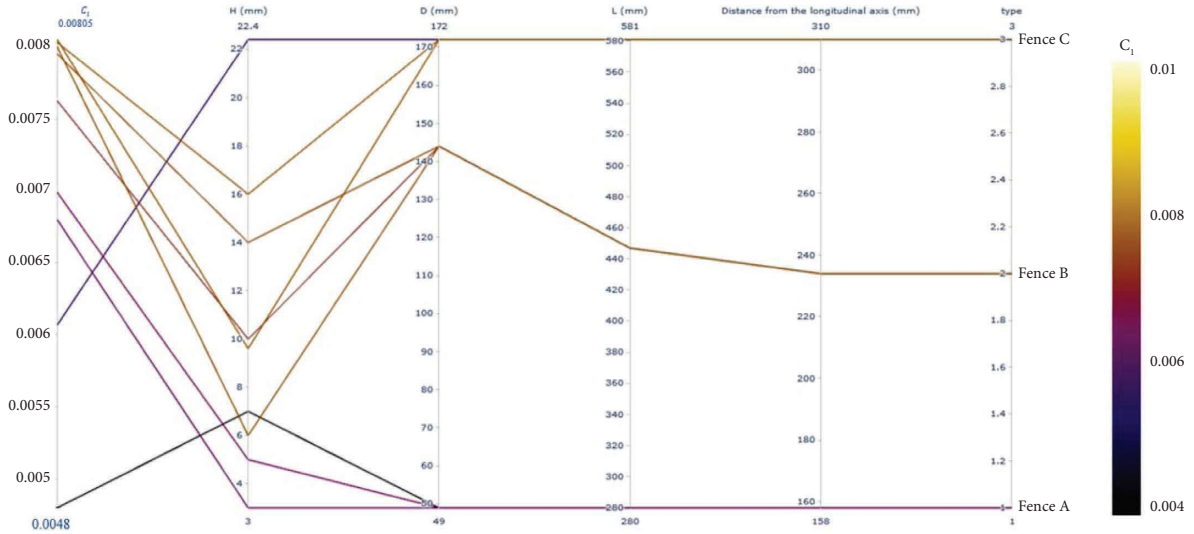

Figure 14: Visualizing the relationship between UAV design and rolling moment coefficient: a parallel coordinate plot.

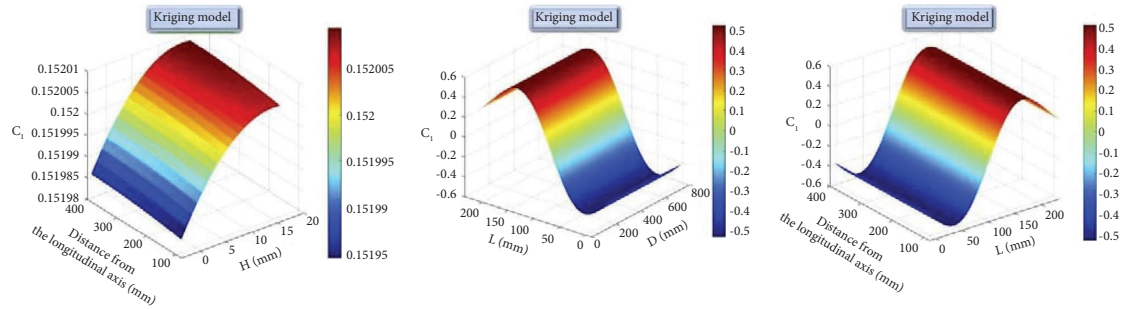

(a) (b) (c)

Figure 15: In these graphs, equation (14) is observed after applying the learning algorithm.

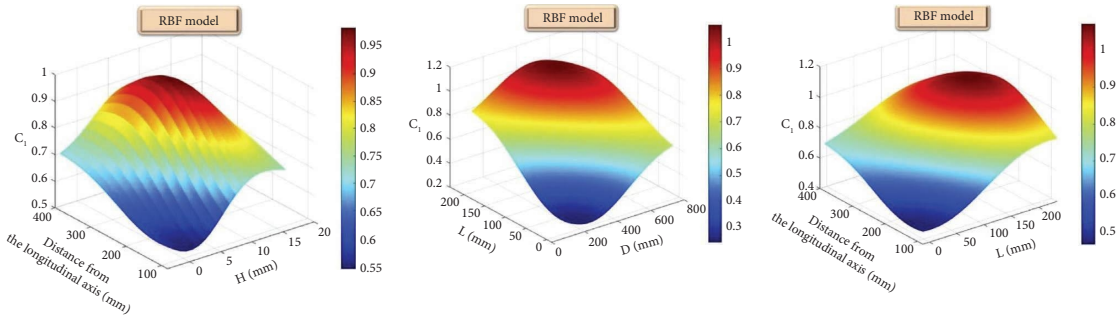

(a) (b) (c)

Figure 16: In these graphs, equation (15) is observed after applying the learning algorithm.

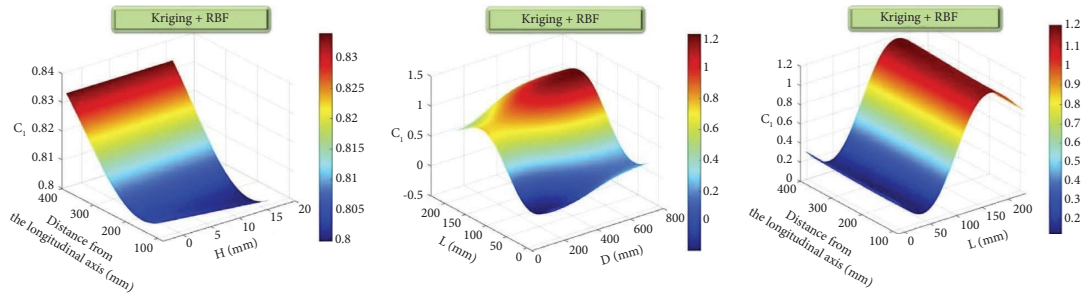

(a) (b) (c)

Figure 17: In the above graphs, equation (1) is observed after applying the learning algorithm.

Table 2: The exact dimensions of the fences created on the UAV wing at three different heights and the optimized point (O) in millimetres.

Fence height (H)			The distance between the fence and the nose of the UAV (D)	The length of the fence (L)	The name of the fence (distance from the longitudinal axis)
70% P	50% P	30% P			
7	5	3	280	49	(158)-A
14	10	6	447	144	(234)-B
22.4	16	9.6	581	172	(310)-C
		7.5	435	121	(236)-O
	13		460	149	(240)-O
18.2			543	163	(290)-O

In Figure 19, you can see that in the optimization of the O fence, the roll coefficient has decreased at a high angle, but at a lower angle of attack, because the vortices are not large, the closer it is to the drag split, the better the result is at the O point. The same thing happened, but it has a slight difference with part C because point O has a better drag coefficient due to its lower length and height compared to C, and finally, it has a better lift-to-drag ratio.

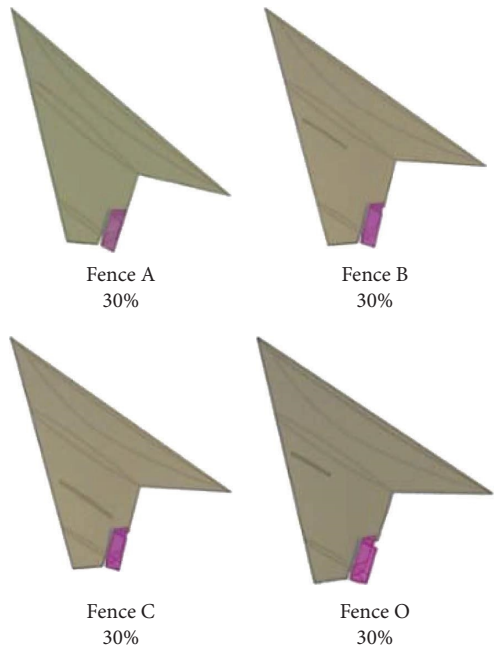

Figure 18: The placement of fences in A, B, C, and O positions.

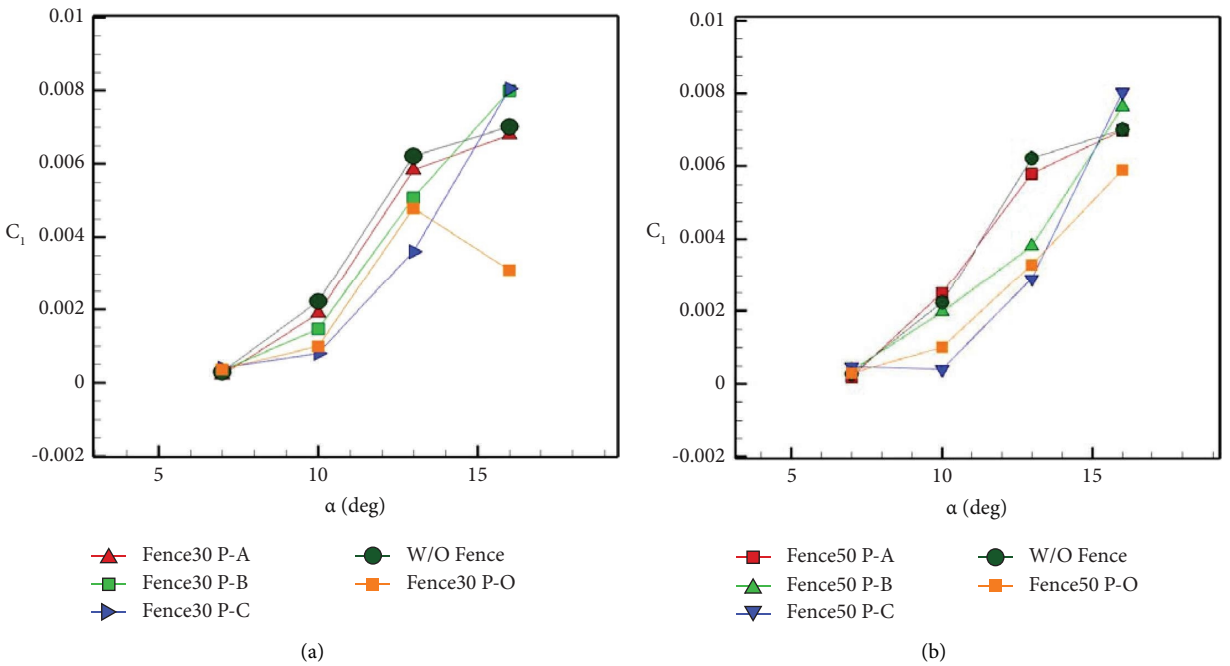

Figure 19: Continued.

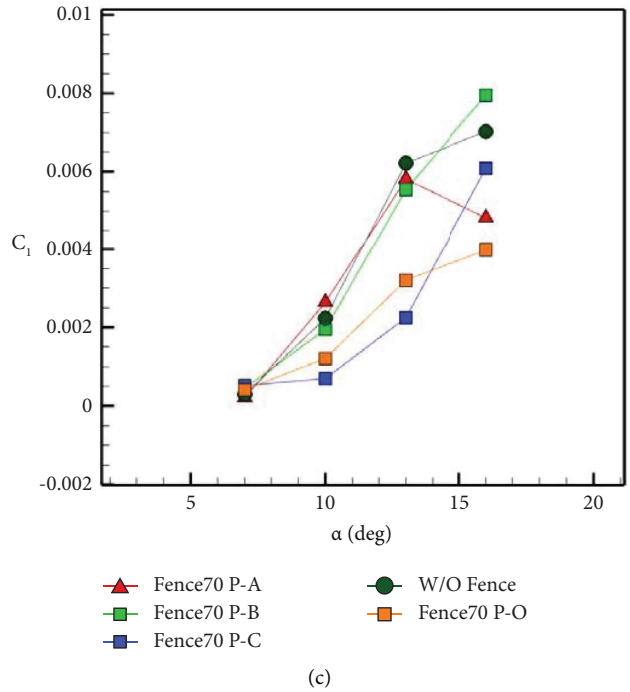

FIGURE 19: A diagram showing different angles of attack *s* in different positions (A, B, C, and O) of the fence. (a) 30% of the vortex diameter, (b) 50% of the vortex diameter, and (c) 70% of the vortex diameter.

6. Conclusion

The researchers developed a genetic algorithm that uses a Kriging model to evaluate the objective function. The Kriging model is a response surface model that represents the relationship between the input and output using a stochastic process. By replacing the CFD analysis solver with the Kriging model, the computational time required for evaluating the objective function was significantly reduced. This approach was useful in designing fences by reducing the number of design variables. Finally, they applied this approach to predict the location of the fence where the rolling coefficient of the aircraft is low and confirmed its efficacy through research findings. Below, you will find a brief explanation of some of the most significant findings from this research:

(i) Placing the fence on swept wings will deflect some of the wing tip vortexes. This means that the fence can help redirect the flow around the wing, reducing the intensity of the vortices formed at the wingtips.

(ii) Using the fence C at low angles of attack (less than 16 degrees) has resulted in a lower roll coefficient when using the split drag system. This indicates that the fence C configuration is effective in reducing rolling motion when the aircraft is at a relatively low angle of attack, improving its stability.

(iii) Vortex formation at high angles of attack with a larger than normal width can cause the fence to sink into the vortex and reduce its performance. This suggests that there are limitations to the effectiveness of the fence under certain conditions, particularly when dealing with high angles of attack and wide vortex formations.

(iv) The use of machine learning to optimize and find the best position of the fence can help prevent it from sinking into the vortex and allow for optimal utilization of the split drag system. Machine learning techniques can analyze various factors and data to identify the most suitable fence position, taking into account factors such as angle of attack, vortex behavior, and overall aerodynamic performance.

Nomenclature

AOA: Angle of attack
C_l: Roll moment coefficients
D: The distance between the fence and the nose of the UAV
H: Fence height
L: The length of the chord of the fence
O: Optimized point
P: Vortex thickness on the wing
RBF: Radial basis function
W/O: Without fence.

Data Availability

The data used in this study are available from the corresponding author upon request.

Conflicts of Interest

The authors declare that they have no conflicts of interest.

References

[1] M. K. Sobhani, M. M. Dehghan, Z. M. Bazaz, and M. Eilbeigi, "F low field over a non experimental investigation of the slender lambda shaped wing by pressure measurement," *Journal of Aeronautical Engineering*, 2015.

[2] N. Qin, A. Vavalle, A. Le Moigne, M. Laban, K. Hackett, and P. Weinerfelt, "Aerodynamic considerations of blended wing body aircraft," *Progress in Aerospace Sciences*, vol. 40, no. 6, pp. 321–343, 2004.

[3] M. Navabi and E. Kakavand, "Combined model-reference adaptive controller for coordinated turn of a tailless aircraft," *Modares Mechanical Engineering*, vol. 15, no. 10, pp. 117–127, 2016.

[4] R. Martinez-Val, "Flying wings. A new paradigm for civil aviation?" *Acta Polytechnica*, vol. 47, no. 1, 2007.

[5] M. Bashir, S. Longtin-Martel, R. M. Botez, and T. Wong, "Aerodynamic design optimization of a morphing leading edge and trailing edge airfoil–application on the uas-s45," *Applied Sciences*, vol. 11, no. 4, p. 1664, 2021.

[6] Z. J. Li and D. L. Ma, "Control characteristics analysis of split-drag-rudder," in *Applied Mechanics and Materials*, vol. 472, pp. 185–190, Trans Tech Publications Ltd, Wollerau, Switzerland, 2014.

[7] G. Stenfelt and U. Ringertz, "Lateral stability and control of a tailless aircraft configuration," *Journal of Aircraft*, vol. 46, no. 6, pp. 2161–2164, 2009.

[8] J. Rajput, W. G. Zhang, and X. B. Qu, "A differential configuration of split drag-rudders with variable bias for directional control of flying-wing," in *Applied Mechanics and Materials*, vol. 643, pp. 54–59, Trans Tech Publications Ltd, Wollerau, Switzerland, 2014.

[9] H. D. Ceron-Muñoz and F. M. Catalano, "Aerodynamic interference of power-plant system on a blended wing body," in *27th International Congress of the Aeronautical Sciences*, Nice, France, January 2010.

[10] N. Namura, S. Obayashi, and S. Jeong, "Efficient global optimization of vortex generators on a supercritical infinite wing20," *Journal of Aircraft*, vol. 53, no. 6, pp. 1670–1679, 2016.

[11] R. Barrett and S. Farokhi, "On the aerodynamics and performance of active vortex generators," in *11th Applied Aerodynamics Conference*, p. 3447, Monterey, CA, USA, August 1993.

[12] D. Liu, B. Song, W. Yang, X. Yang, D. Xue, and X. Lang, "A brief review on aerodynamic performance of wingtip slots and research prospect," *Journal of Bionics Engineering*, vol. 18, no. 6, pp. 1255–1279, 2021.

[13] W. A. Newsom Jr, D. R. Satran, and J. L. Johnson Jr, "Effects of wing-leading-edge modifications on a fullscale, low-wing general aviation airplane: wind-tunnel investigation of high-angle-of-attack aerodynamic characteristics (No. L-15101)," 1982, https://ntrs.nasa.gov/citations/19820018341.

[14] J. K. Dickson and F. B. Sutton, "The effect of wing height on the longitudinal characteristics at high subsonic speeds of a wing-fuselage-tail combination having a wing with 40 degrees of sweepback and NACA four-digit thickness distribution (No. NACA-RM-A55C30)," 1955, https://ntrs.nasa.gov/citations/19930088986.

[15] C. Papadopoulos, S. Ioannidou, P. Panagiotou, and K. Yakinthos, "Numerical investigation of the impact of tubercles and wing fences on the aerodynamic behaviour of a fixed-wing, tactical Blended-WingBody UAV platform," in *IOP Conference Series: Materials Science and Engineering*, vol. 1226, IOP Publishing, Salerno, Italy, February, 2022.

[16] A. C. Demoret, "The effect of passive and active boundary-layer fences on delta wing performance at low Reynolds number," Technical Report, Air Force Institute of Technology, Wright-Patterson Air Force Base, OH, USA, 2020.

[17] V. Esfahanian, M. J. Izadi, H. Bashi, M. Ansari, A. Tavakoli, and M. Kordi, "Aerodynamic shape optimization of gas turbines: a deep learning surrogate model approach," *Structural and Multidisciplinary Optimization*, vol. 67, no. 1, p. 2, 2024.

[18] F. Li, Z. Shang, Y. Liu, H. Shen, and Y. Jin, "Inverse distance weighting and radial basis function based surrogate model for high-dimensional expensive multi-objective optimization," *Applied Soft Computing*, vol. 152, Article ID 111194, 2024.

[19] F. Pazooki, A. Zibafar, and M. Rahmati Lish, "Optimization and design of general aviation aircrafts wing using non-dominated sorting genetic algorithms ii," *Journal of Aeronautical Engineering*, vol. 23, no. 2, pp. 100–115, 2021.

[20] R. Perez, H. Liu, and K. Behdinan, "Flight Dynamics and control multidisciplinary integration in aircraft conceptual design optimization," in *10th AIAA/ISSMO Multidisciplinary Analysis and Optimization Conference*, p. 4435, New York, NY, USA, June 2004.

[21] A. Ghorbani and S. Malaek, "Airplane conceptual design based on genetic algorithm," *Journal of Mechanical and Aerospace Engineering*, vol. 1, 2005.

[22] J. Yoon, N. Nguyen, S. M. Choi, J. W. Lee, S. Kim, and Y. H. Byun, "Multidisciplinary general aviation aircraft design optimizations incorporating airworthiness constraints," in *10th AIAA Aviation Technology, Integration, and Operations (ATIO) Conference*, p. 9304, Fort worth, TX, USA, June 2010.

[23] G. G. Wang and S. Shan, "Review of metamodeling techniques in support of engineering design optimization," in *International Design Engineering Technical Conferences and Computers and Information in Engineering Conference*, Philadelphia, PA, USA, September 2007.

[24] M. A. Oliver, "An overview of geostatistics and precision agriculture," *Geostatistical applications for precision agriculture*, pp. 1–34, Springer, Berlin, Germany, 2010.

[25] J. P. Chilès and N. Desassis, "Fifty years of kriging," *Handbook of mathematical geosciences: fifty years of IAMG*, pp. 589–612, Springer, Berlin, Germany, 2018.

[26] N. Petcharat, A. Wiangkham, A. Pichitkul et al., "The multi-objective optimization of material properties of 3D print onyx/carbon fiber composites via surrogate model," *Materials Today Communications*, vol. 37, Article ID 107362, 2023.

[27] X. Zhao, Y. Yang, and X. Ma, "Kriging aerodynamic modeling and multi-objective control allocation for flying wing UAVs with morphing trailing-edge," *IEEE Access*, vol. 9, pp. 62394–62404, 2021.

[28] M. Tomac and G. Stenfelt, "Predictions of stability and control for a flying wing," *Aerospace Science and Technology*, vol. 39, pp. 179–186, 2014.

[29] R. Karimi Kelayeh and M. H. Djavareshkian, "Aerodynamic assessment of a control strategy based on twist morphing wing in a flying wing aircraft," *Journal of Aerospace Engineering*, vol. 37, no. 1, Article ID 04023087, 2024.